Nonlinear Modeling of the Effect of n=2 Resonant Magnetic Field Perturbation on Peeling-Ballooning Mode in KSTAR

S.K. Kim[1], S. Pamela[2], O. Kwon[3], M. Becoulet[4], G. T. A. Huijsmans[4,5], Y. In[6] , M. Hoelzl[7], J. H. Lee[8], M. Kim[8], G.Y. Park[8], H. S. Kim[8], Y.H. Lee[1], G.J. Choi[9], C.Y. Lee[1], A. Kirk[2], A.Thornton[2], JOREK team and Y.–S. Na[1*]

[1]Department of Nuclear Engineering, Seoul National University, Gwanak 08826, Seoul, Korea

[2]CCFE, Culham Science Centre, Abingdon, Oxon OX14 3DB, United Kigdom

[3]Department of Physics, Daegu University, Gyeongsan 38453, Gyeongbuk, Korea

[4]CEA, IRFM, 13108 Saint-Paul-Lez-Durance, France

[5]Eindhoven University of Technology, Eindhoven, The Netherlands

[6]Ulsan National Institute of Science and Technology, Ulsan, Korea

[7]Max Plank Institute for Plasma Physics, 85748 Garching, Germany

[8]National Fusion Research Institute, Youseong 34133, Daejeon, Korea

[9]Department of Physics and Astronomy, University of California, Irvine, California 92697, USA

Abstract

Using the nonlinear 3D MHD code JOREK with reduced MHD equations (viscos-resistive MHD), we have successfully simulated a recent n=2 RMP-driven ELM suppression in KSTAR. We have found that such ELM suppression has been attributable not only to the degraded pedestal but also to the direct coupling between peeling-ballooning mode (PBM) and RMP-driven plasma response. Notably, the pedestal pressure gradient is reduced as the radial transport is enhanced because of the formation of the stochastic layer and increased convection fluxes due to tearing and kink-peeling mode (KPM) driven by RMPs. The increased transport in the stochastic layer is due to the parallel transport across the stochastic fields, described by the Braginskii model in the simulation. While the linear stability of PBM improves owing to the degraded pedestal, it is not a sole contributor to ELM suppression, in that the nonlinear mode coupling plays a more critical role. This outcome is consistent with the previous studies where mode coupling affects the ELM mitigation or suppression. In addition, the locking of PBM has been numerically achieved during the ELM suppression phase, which may support the relationship between $V_{E \times B} \approx 0$ at the pedestal and the onset of ELM suppression. We suggest that locking of PBM can enhance the mode interactions between RMPs and PBMs, which is significant to ELM suppression.

1. Introduction

The high confinement plasma operation mode (H-mode) is one of the candidates for fusion plasma operations in ITER. The H-mode plasma is characterized by having an edge transport barrier. The edge transport barrier is generally understood to occur when the E×B shearing rate, which stabilises

turbulence [1, 2], exceeds a critical threshold in the edge region. As a result of the edge transport barrier, a pedestal forms at the edge, leading to an overall increase of the plasma confinement [3] via profile stiffness [3]. However, the high pressure gradient in the pedestal and subsequent high edge bootstrap current density can cause so-called Edge Localized Modes (ELM). Peeling-ballooning modes (PBM) [4, 5], driven by current density (peeling) and pressure gradient (ballooning), are considered the dominant MHD instability resulting in ELM. ELMs induce the periodic collapse of the pedestal and release transient heat fluxes to the plasma-facing components, which can result in significant heat loads on the divertor targets. In future devices such as ITER and DEMO, divertor heat fluxes during ELMs are expected to exceed the order of a few GW/m^2 [6, 7], which can cause severe damage to tungsten divertor tiles. Therefore, a reliable way to control or suppress ELMs is essential for the high-performance steady state operation based on the H-mode regime.

Resonant magnetic perturbations (RMPs) using external magnetic coils are one of the effective ways of suppressing ELMs. It has been found that RMPs can fully suppress ELMs in DIII-D [8], KSTAR [9], EAST [10], and ASDEX Upgrade [11]. In addition, there are reports on ELM mitigation using RMPs in JET [12] and MAST [13]. The 'initial understanding' (or 'initial hypothesis') of RMP-driven ELM suppression is as follows: When RMPs of toroidal mode "n" are applied, the field perturbations penetrate into the plasma and induce magnetic islands at the rational surfaces with q=m/n, where m and n denote the poloidal and toroidal mode numbers, respectively. Because the rational surfaces are sufficiently dense at the plasma edge, the islands can overlap each other to form a stochastic layer and increase radial transport. Increased radial transport in the stochastic layer can occur due to parallel transport across the stochastic fields, described by the Braginskii model. As a result, the ELM is suppressed as the pedestal slope remains below the marginal stability limit. In this respect, extensive research on field penetration and radial transport by RMPs has been carried out [14-20]. They have revealed that perpendicular electron flow shields RMPs and a zero electron flow layer is important for full field penetration in the pedestal. Numerical studies have shown that RMPs can drive a kink-peeling response in the plasma and amplify field penetration [21-24]. Here, this response can form an ExB convective flux that further reduces the density pedestal gradient by increasing the radial transport in the edge region. It has also been reported that RMPs can increase turbulence transport in the pedestal [25, 26]. These studies attempted to explain RMP-driven ELM suppression with pedestal degradation, but have certain limitations in explaining the experimental observation where coherent PBM-like mode structures with n different from that of RMPs remain during the ELM suppression phase. To understand the results of these experiments, several studies have focused on the direct coupling between RMPs and ELMs. They found that the properties and stability of PBM change with 3D-field modulation by RMPs [27, 28].

In this paper, the plasma response and PBM suppression by RMPs have been studied. The RMP driven

ELM suppression discharge in KSTAR is modeled with the 3D nonlinear MHD code JOREK [29]. Descriptions of the model and experimental observation are given in section 2. Section 3 describes "natural" PBM simulations without RMPs. In sections 4 and 5, modelling results for the plasma response and suppression of PBM induced by RMPs are presented, respectively. A possible mechanism of ELM suppression, including nonlinear interactions between RMPs and PBMs, is also discussed. Last, the conclusion is drawn in section 6.

2. Configuration of the simulation

2-1. Simulation model

We used JOREK, a 3D nonlinear MHD code with X-points and scrape-off-layer (SOL) [7]. The reduced MHD model based on five field equations is used, including Ohm's law, the continuity equation, the momentum equation, and the energy equation. Momentum equations are divided into parallel and perpendicular components. The realistic toroidal flow, two-fluid diamagnetic effect, and the neoclassical viscosity are included to describe the effect of plasma flow on the ballooning mode [17, 19].

In the JOREK code, the magnetic field is expressed as $\vec{B} = F_0 \nabla \phi + \nabla \psi \times \nabla \phi$, where ϕ is the toroidal angle, ψ is the poloidal magnetic flux, and $F_0 = R_0 B_{\phi 0}$. R_0 is the magnetic axis, and $B_{\phi 0}$ is the amplitude of the toroidal field at $R = R_0$. F_0 is constant in time, and ϕ increases clockwise in the simulation.

The plasma fluid velocity $\vec{V}$ is expressed as Eq. (1)

$$\vec{V} \approx \vec{V}_{||} + \vec{V}_{\mathrm{E}} + \vec{V}_{\mathrm{i*}}, \tag{1}$$

where $\vec{V}_{||}$ is the velocity parallel to the magnetic field, and $\vec{V}_{\mathrm{E}} = \vec{E} \times \vec{B}/B^2$ is the $\vec{E} \times \vec{B}$ drift velocity. The electric field is expressed as $\vec{E} = -\nabla u$, where u is the electrostatic potential. $\vec{V}_{\mathrm{i*}} = -\nabla P_{\mathrm{i}} \times \vec{B}/(\rho e B^2/m_i)$ is the ion diamagnetic velocity that reflects the two-fluid diamagnetic effect. Here, P_{i}, e, m_{i}, and $\rho(= m_{\mathrm{i}} \times n_{\mathrm{i}})$ are the scalar pressure, charge, mass, and mass density of ion, respectively. The density of ion and electron is assumed to be $n_{\mathrm{i}} = n_{\mathrm{e}}$. We also set $T_{\mathrm{i}} = T_{\mathrm{e}} = T/2$ and $P_{\mathrm{i}} = P_{\mathrm{e}} = P/2$ for simplicity, where T and P are the sum of ion and the electron temperatures and scalar pressures, respectively. The normalized set of five field equations [19] is:

$$\frac{1}{R^2}\frac{\partial \psi}{\partial t} = -\vec{B} \cdot \left(\nabla u - \frac{\tau_{IC}}{\rho} P \right) + \eta \nabla \cdot \left(\frac{1}{R^2} \nabla_\perp \psi - j_s \right), \tag{2}$$

$$\frac{\partial \rho}{\partial t} = -\nabla \cdot \left(\rho \vec{V} \right) + \nabla \cdot \left(D_\perp \nabla_\perp \rho \right) + S_\rho, \tag{3}$$

$$\nabla\phi \cdot \nabla \times \begin{bmatrix} \rho(\partial_t + \vec{V}\cdot\nabla)\vec{V}_E + \nabla(\rho T) - \vec{j}\times\vec{B} \\ +\nabla\cdot\overleftrightarrow{\Pi}_{i,neo} + \vec{S}_V - \vec{V}S_\rho - \nu_\perp\nabla^2\vec{V} \end{bmatrix} = 0, \tag{4}$$

$$\vec{B}\cdot\begin{bmatrix} \rho(\partial_t + \vec{V}\cdot\nabla)\vec{V}_{||} + \nabla(\rho T) - \vec{j}\times\vec{B} \\ +\nabla\cdot\overleftrightarrow{\Pi}_{i,neo} + \vec{S}_V - \vec{V}S_\rho - \nu_{||}\nabla^2\vec{V} \end{bmatrix} = 0, \tag{5}$$

$$\frac{\partial(\rho T)}{\partial t} = -(\vec{V}_E + \vec{V}_{||})\cdot\nabla(\rho T) - \gamma\rho T\nabla\cdot(\vec{V}_E + \vec{V}_{||}) + \nabla\cdot(\kappa_\perp\nabla_\perp T + \kappa_{||}\nabla_{||}T)$$
$$+ (1-\gamma)S_T + V^2 S_\rho/2, \tag{6}$$

The variables are normalized as follows: $\rho = \rho_{SI}/\rho_{0,SI}$ and $t = t_{SI}/\sqrt{\mu_0\rho_{0,SI}}$, where SI represents the SI unit value, $\mu_0 = 4\times10^{-7}$, and $\rho_{0,SI}$ is mass density on the magnetic axis. The normalization of the other variables is $p = \mu_0 p_{SI}$, $T = \mu_0\rho_{0,SI}(e/m_i)T_{SI}$, $j = \mu_0 j_{SI}$, and $u = u_{SI}\sqrt{\mu_0\rho_0}/F_{0,SI}$. j is the plasma current density. The flow is normalized to $V_{||} = V_{||,SI}\sqrt{\mu_0\rho_0}/B_{SI}$ and $V_\theta = \vec{V}\cdot\hat{e}_\theta = V_{\theta,SI}/\sqrt{\mu_0\rho_0}$, depending on the direction. Here, the poloidal unit vector $\hat{e}_\theta$ is defined as

$$\hat{e}_\theta = \frac{R}{\nabla\psi}(\nabla\psi\times\nabla\phi). \tag{7}$$

A Spitzer-like resistivity $\eta = \eta_{0,SI}\sqrt{\rho_{0,SI}/\mu_0}(T_e/T_{e,0})^{-3/2}$, temperature-dependent perpendicular viscosity $\nu_\perp = \nu_{\perp0,SI}\sqrt{\rho_{0,SI}\mu_0}(T_e/T_{e,0})^{-3/2}$, and constant parallel viscosity $\nu_{||} = \nu_{||,SI}\sqrt{\rho_{0,SI}\mu_0}$ are used in the modeling. Here, $\eta_{0,SI}$, $\nu_{\perp0,SI}$, and $T_{e,o}$ are the resistivity, perpendicular viscosity, and electron temperature on the magnetic axis, respectively. Braginskii parallel conductivity $\kappa_{||} = \kappa_{||0,SI}\sqrt{\rho_{0,SI}\mu_0}(T_e/T_{e,0})^{5/2}$ and adiabatic index $\gamma = 5/3$ are also applied. Particle source S_ρ and the heat source S_T, as well as the perpendicular particle diffusion coefficient $D_\perp = D_{\perp SI}\sqrt{\rho_{0,SI}\mu_0}$ and thermal diffusion coefficient $\kappa_\perp = \kappa_{\perp SI}\sqrt{\rho_{0,SI}\mu_0}$ are set to maintain the initial density and temperature profiles. Their typical values on the magnetic axis are $D_{\perp0,SI} \approx 1cm^2/s$ and $\kappa_{\perp0,SI} \approx 1kg/(m\cdot s)$. $D_\perp$ and $\kappa_\perp$ vary radially. Their radial profiles are proportional to $D_\perp \propto |\nabla\rho|^{-1}$ and $\kappa_\perp \propto |\nabla T|^{-1}$ of initial ρ and T profiles. In addition, the current source j_A and the toroidal momentum source $\vec{S}_V$ are applied to reproduce the realistic equilibrium profile. All source profiles remain the same over time.

The neoclassical poloidal friction has the heuristic form [30] as

$$\nabla\cdot\overleftrightarrow{\Pi}_{i,neo} = \rho\mu_{i,neo}\frac{B^2}{B_\theta^2}(V_\theta - V_{\theta,neo})\hat{e}_\theta, \tag{8}$$

where $B_\theta = \vec{B}\cdot\hat{e}_\theta$, $V_{\theta,neo} = k_i\tau_{IC}(\nabla_\perp\psi\cdot\nabla_\perp T)/B_\theta$, $\mu_{i,neo} = \mu_{i,neo,SI}\sqrt{\mu_0\rho_0}$, and $\tau_{IC} = m_i/(2eF_0\sqrt{\mu_0\rho_0})$. The neoclassical coefficients $\mu_{i,neo}$ and k_i are calculated from Ref [31]. Using these models, the plasma flows develop toward equilibrium, and plasma is finally obtained in which the

flows and electric field satisfy the radial force balance. The radial electric field can be written as Eq. (9)

$$E_r = \frac{1}{en}\frac{\partial P_i}{\partial r} + B_\phi V_\theta - B_\theta V_\phi. \tag{9}$$

[32], where ∂_r is the radial gradient and V_ϕ is the toroidal plasma flow.

In JOREK, 2D cubic Bezier finite elements are used to construct a 2D grid in a poloidal cross-section [33], and the toroidal direction is decomposed into the Fourier series. Finite element grids align to equilibrium flux surfaces that include core, SOL, and the private region. The boundary of the computational domain is limited by the flux surfaces and divertor target plates. For the boundary condition of the computational domain, the Dirichlet condition is used for all variables except the divertor targets. On the divertor targets, the temperature and the density have free outflow, and Bohm sheath boundary conditions are applied [32]. The implicit Crank–Nicolson scheme is used for time stepping. The sparse system of equations is solved using Generalized Minimal REsidual Solver (GMRES) with a preconditioner obtained by solving each submatrix independently corresponding to non-coupled Fourier harmonics. These sub-matrices are solved using PaStiX [34], the direct parallel sparse matrix solver.

2-2. Input configuration

We use the data from KSTAR #18594 discharge [35] of n=2 RMP driven ELM suppression. The main parameters of this discharge are shown in Figure 1; major radius ($R_0 = 1.8$ m), toroidal field ($B_{\phi 0} = 1.8$ T), plasma current ($I_p = 0.66$ MA), q profile with central $q_0(\sim 1)$, $q_{95}(\sim 3.8)$, global poloidal beta ($\beta_p \sim 1$), and line average density ($\bar{n}_e \sim 3.3 \times 10^{19}$ m^{-3}). In this discharge, the currents in the three rows of versatile in-vessel control coils (IVCC) with two turns in the low field side [9] were set such that the magnetic perturbation of n=2 was applied. Due to the geometry of IVCC, small sideband modes such as n=4,6,8, etc., were induced, but they are ignored in this study because they are much smaller than the amplitude of the n=2 component. The phase difference between the rows was $\Delta\Phi = 90°$, and it is the standard n=2 field coil configuration for suppressing ELMs in KSTAR. When the stationary state was reached (~ 4.9 s), RMP with the coil current $I_{RMP} = 2$ kA was applied from 5.0 s to 5.5 s and then gradually increased with the rate of ~ 0.2 kA/s. ELM suppression was achieved at 13.0 s with $I_{RMP} \sim 3.7$ kA. This full suppression lasted until the end of the discharge. We note that I_{RMP} is defined as twice the current applied in the actual experiment because the coil is wound in two turns. In the simulation, t = 6.45 s, the earliest time slice when electron cyclotron emission imaging (ECEI) measurement [36, 37] becomes available, is selected as a reference time. At this point, the profile variation and ELM mitigation due to RMP have not yet appeared. For this reference, ELMy plasma equilibrium is reproduced, and simulation results are compared with the ECEI measurement.

We performed the axisymmetric equilibrium reconstruction with the EFIT code [38]. It is noteworthy that the tokamak system becomes no longer axisymmetric when 3D fields are applied. So 3D equilibrium reconstruction of tokamaks is also valuable for the study on the effect of RMP [39-41]. Initial temperature and density profiles were fitted from charge exchange spectroscopy (CES) and Thomson scattering (TS) diagnostic data considering error bars. Here, the kinetic profile from CES was slightly shifted (~5 mm) to align with the magnetic equilibrium separatrix. The resulting q, n_e, T_e, T_i, and toroidal rotation V_ϕ profile are shown in Figure 2. The electron density and the temperature profile in the pedestal region have considerable uncertainty due to the low spatial resolution and large error bars of the TS measurement in the plasma edge. For these reasons, the n_e and T_e pedestal profiles are adjusted to improve quality in the simulation. The profiles are changed within the error bars to make the equilibrium linearly unstable to PBM and to match the mode properties of ECEI and diamagnetic loop measurements. The change in PBM linear stability, the most dominant n, and the ELM energy loss are calculated by changing the width and height of the n_e and T_e pedestal simultaneously, as in Ref [42]. The modified Sauter model [43] is used to calculate the edge bootstrap current. In this scan, the neoclassical bootstrap current is re-computed to be self-consistent with the pressure profile. First, the linear stability is analyzed and the most dominant n is checked by the ideal MHD code, MISHKA1 [44], with a simplified ion diamagnetic effect [45]. The result is shown in Figure 3. The orange star represents the reference pedestal, the pink line is the marginal PBM stability limit, and the red line corresponds to the pedestal whose dominant PBM mode is $n = 12$, consistent with the ECEI measurement. The linear growth rate (γ) increases with the height, while it decreases with the width, and the dominant n decreases as increasing γ. With this exercise, the linear instability and the most dominant n constraints are satisfied by increasing the pedestal height by 5-12% (see the pink star in Figure 3). We note that JOREK is a resistive MHD code, so its result may differ from that with the ideal MHD model. Another constraint is the ELM energy loss which requires nonlinear calculations. Thus, JOREK calculations are performed. It is found that the measured ELM energy loss can be achieved in the simulation by increasing the pedestal height by $\sim 10\%$. Detailed nonlinear calculation results are given in section 3. The final equilibrium has n_e and T_e pedestal heights 10% higher than the original reconstruction (see the green star in Figure .3). As mentioned earlier, it is still within the measurement error bars. After the static equilibrium with n_e, T, and V_ϕ is constructed, the neoclassical coefficients of Ref [31] are calculated as shown in Figure 4(a). E_r satisfying Eq. (9) is found by evolving only n=0 component by $t = 2000\tau_\mathrm{A}$. The poloidal flow profiles from the resulting E_r and the distribution of $V_{||}$ are shown in Figure. 4(b) and (c), respectively. This process reproduces the self-consistent kinetic equilibrium with plasma flow based on experimental data.

We used normalized parameters based on the experimental data; $\kappa_{||0} = 2 \times 10^3$ ($\kappa_{||0,\mathrm{SI}} = 4.5 \times 10^9$ m^{2}s^{-1}), $\nu_{\perp0} = 2 \times 10^{-7}$ ($\nu_{\perp0,\mathrm{SI}} = 4.5 \times 10^{-1}$ m^{2}s^{-1}), and $\nu_{||} = 2 \times 10^{-6}$ ($\nu_{||,\mathrm{SI}} =$

4.5 m^2s^{-1}). Here, for numerical reasons, 40 times larger resistivity ($\eta_0 = 2 \times 10^{-7}$, $\eta_{0,\text{SI}} = 5.7 \times 10^{-7}$ Ωm) and two times smaller $\tau_{\text{IC}}(= 3 \times 10^{-3})$ are used, and this is one of the important limitations of this study.

3. PBM simulation without RMP effect

In order to study the ELM suppression by RMPs, it is essential to check if PBMs occur while without RMP to be consistent with the experimental data. For this purpose, the linear PBM stability of the initial phase is checked. In our reference time slice (6.45 s), when the effect of RMP was minimal or has not yet effective, the n of the most unstable PBM was 12 in the linear phase from ECEI diagnostics. The temperature fluctuation, δT_e, for the n = 12 PBM inside separatrix with $\Delta t \sim 60$ μs ($= 120\tau_A$) is presented in Figure 5 (a), where $\langle \cdots \rangle$ means time averaged value. In the measurement, the mode structure was poloidally rotating in the ion-diamagnetic direction (-z direction at LFS) with $V_{\theta,\text{mode,exp}} \sim 2.9$ km/s in the lab frame. To calculate the linear behavior of PBM, a single harmonic with n=12 is launched on the kinetic equilibrium with a small amplitude at the numerical noise level ($\sim 10^{-27}$) in the JOREK unit. Then, the linear phase of PBM is modeled. Its linear growth rate is $\gamma\tau_A \sim 0.054$. The resulting δT_e for n=12 PBM at LFS in the lab frame corresponds to Figure 5 (b). Here, δT_e is taken near the end of the linear phase with $\Delta t \sim 55$ μs ($= 110\tau_A$), and $\langle T_e \rangle$ is derived from its background (n=0) value. In the figure, the n=12 mode structure rotates in the ion-diamagnetic direction at about $V_{\theta,\text{mode}} \sim 3.2$ km/s, which shows good agreement with the ECEI measurement (~ 2.9 km/s). It is noteworthy that $V_{\theta,\text{mode}}$ is similar to $V_{\theta,E}(\sim 2.8$ km/s) at the mode location. In our case, the poloidal $E \times B$ velocity $V_{\theta,E} = \hat{e}_\theta \cdot \vec{V}_E$ at the pedestal is in the ion-diamagnetic direction due to large V_ϕ [32], and therefore modes rotate in the clockwise direction. This similarity between $V_{\theta,\text{mode}}$ and $V_{\theta,E}$ is also consistent with the previous studies [32, 46].

As ELM is not a single mode event but a nonlinear MHD phenomenon, the mode coupling should be considered in the modeling. Therefore, the nonlinear simulation including multi harmonics is conducted for the next step. Although n=12 is the most unstable mode, harmonics of n=2, 4, 6, 8, 10, 12, and 14 have been considered within the limits of the computational resources. The results for the perturbed kinetic energy $W_{\text{kin}} = \int \rho |\nabla_\perp u|^2 dV/2$ of PBM in the nonlinear phase are shown in Figure 6. Here, n=12 is the fastest growing mode so to enter the nonlinear phase first. Then, other modes including n=10 are driven by mode coupling in the nonlinear phase [47], which result in a bursty MHD behavior with mode crashes. For example, the amplitude of n=10 mode increases during the n=12 mode crash. The n=10 mode starts to crash $700\tau_A$ after the crash of the n=12 mode. During the mode crash, the nonlinear Maxwell stress induces the strong shear of the plasma filaments. As a consequence, thermal energy and particles are expelled across the separatrix, resulting in flows and shearing-off of the large

heat flux across SOL [32, 48]. Figure 6(b) shows the change of density and temperature pedestal at $\sim 3500\tau_A$ from the simulation. Both pedestals are collapsed as the PBM crashes occur. For example, heights of density and temperature pedestal decreased by 26% and 21%, respectively. The stored energy also decreased by $\Delta W_{ELM,Sim} \approx 8.1$ kJ, which is close to the experimental value $\Delta W_{ELM,Exp} \approx 7(\pm 2)$kJ. Because the magnitude of the crash increases with the mode amplitude in the nonlinear phase, the ELM size also increases with W_{kin}. Therefore, the largest perturbed kinetic energy during the nonlinear phase, $W_{kin,max}$, is used to estimate the size of PBM or ELM in the later sections.

4. Effects of RMP on the plasma equilibrium

4-1. Kink-tearing plasma response in the presence RMP

We examined the response of plasma equilibrium (n=0 component) under the RMP application. RMP in JOREK simulations is treated with a similar approach as in Ref [19]. The vacuum RMP field for a given configuration is calculated with the ERGOS code [49]. The computed boundary and vacuum flux for the n=2, $I_{RMP} = 4$ kA, and odd RMP configuration are applied as boundary conditions on the computational domain for the ψ perturbation. Here, the vacuum approximation is used because the boundary of the computational domain is far away from the separatrix. The perturbed boundary condition is gradually established during $300\tau_A$. In this way, the penetration of the magnetic perturbation into the plasma is evaluated self-consistently.

As the plasma response after RMP application is investigated in this section, only n=0 (equilibrium) and n=2 (RMP) harmonics are included in the modeling. The simulation shows nonlinear plasma response including changes of both n=0 and n=2 components. Here, we consider n = 2 plasma response as a harmonic component that is different from the main PBM. When RMP is established, the plasma perturbations are observed. The perturbed poloidal flux, density, and temperature are presented in Figure 7(a), (b), and (c), respectively. As RMP penetrates the plasma, n=2 perturbations with m=7-14 occur in the edge region. Larger perturbations of temperature and density are observed at the X-point. In order to identify this response, the linear displacement ξ_{lin} is calculated from Ref [23], and this mode has an edge localized structure as shown in Figure 8 with kink-peeling mode (KPM) characteristics [22-24, 50]. Note that the n=2 mode is linearly stable in our case so RMP could linearly drive the n=2 KPM. This result is consistent with the previous studies where peeling-like mode was observed in the response under RMP [51-53]. Interestingly, a perturbed radial $E \times B$ flow is generated at the edge region due to KPM. It results in n=0 conductive flux, $\Gamma_{E \times B}$, in the radial direction. The distribution of $\Gamma_{E \times B}$ driven by KPM can be found in Figure 7(d). A large $\Gamma_{E \times B}$ layer exists at $\psi_N = 0.98 - 1.0$ and is widely distributed poloidally. It has the largest value near the X-point, which agrees with the mode structure of KPM. This widely distributed $\Gamma_{E \times B}$ increases radial transport in the pedestal.

The formation of the particle and heat convection flux is also consistent with similar numerical studies [54, 55].

In addition to the KPM-like plasma response, magnetic islands can be formed due to RMP field penetration. However, the plasma shielding current that suppresses the field penetration can be generated, which reduces the island size. This shielding effect is the result of the plasma flow and the low resistivity of the core plasma [14-20]. RMP cannot penetrate the plasma when plasma has zero resistivity or infinite rotation [56, 57]. The calculated field penetration is given in Figure 9. Fourier decomposed perturbed poloidal flux (Figure 9(a)) and the plasma current (Figure 9(b)) are plotted on the poloidal mode number versus ψ_N space. The field penetration is almost blocked on the rational surface (red line) due to the formation of the shielding current at each resonant surface. Therefore, only small islands remain in the core region. On the other hand, significant field penetration is observed in the edge region. Because plasma resistivity is relatively large in this region, the perturbed current cannot entirely shield the external field [17]. Also, a layer with zero perpendicular flow, $V_{\perp,e} \approx 0$, exists at the rational surface near $\psi_N = 0.95$ which corresponds to the pedestal top in our case. The external field can fully penetrate into this region [15, 18-20] and generate large magnetic islands. Furthermore, the magnetic perturbation is amplified by the poloidal coupling with the kink component, and KPM enhances the field reconnection at the plasma boundary [24, 58]. Therefore, the large island can remain in the pedestal region, and the stochastic layer is formed by the overlap of islands. This can be clarified in the Poincare plot in Figure 10. Here, θ_{geo} is defined as

$$\theta_{geo} = \tan^{-1} \left[\frac{Z - Z_0}{R - R_0} \right], \tag{10}$$

where Z_0 is the location of the magnetic axis in the (R, Z) coordinate. In this plot, large island structures at the resonant surfaces (q= 7/2 and 8/2) near the pedestal top are found while the island size at the inner region (q=6/2) is much smaller. A secondary island structure is also generated at q=11/4. For $0.95 \leq \psi_N \leq 1.0$, the stochastic layer exists, which can increase the radial transport. In this work, the radial transport in the stochastic layer can increase due to the parallel transport described by the Braginskii model.

In summary, KPM and the magnetic islands occur as a plasma response under the external field perturbation. This generates the convection and the stochastic layer in the pedestal region, which can lead to increased radial transport.

4-2. Mean profile variation with RMP

Increased radial transport due to tearing and kink-peeling response to RMP can lead to degradation of the mean (n=0) pedestal gradient and stabilization of edge MHD modes. To investigate the variation of the mean profile under RMP, plasma responses to $0 \leq I_{RMP} \leq 4$ kA are calculated. Figure 11(a) shows the degradation of mean pedestal profiles of the density and the temperature. As the amplitude of the RMP field increases, the gradient of both n_e and T pedestal decreases. For example, ∇n_e and ∇T at the center of the pedestal ($\psi_N = 0.98$) decrease by 58% and 39%, respectively, as $I_{RMP} = 4$ kA is applied. Here, the yellow and the green colored region correspond to the stochastic layer and the location of the convection ($\Gamma_{E \times B}$) layer at the midplane of LFS, respectively. The overall degradation of n_e and T pedestal appears in the stochastic layer because of the increased radial transport. In the convection layer, on the other hand, the change in n_e pedestal is significant while that of T pedestal is small. This implies that $\Gamma_{E \times B}$ which is driven by KPM has a more significant impact on particle transport. 80% of the total radial particle flux at the center of the pedestal is due to $\Gamma_{E \times B}$. Experimental findings show that the density pump-out under RMP is highly correlated with the X-point deformation [22, 59]. Because KPM makes large displacement at the X-point, it may play an important role in the density pump-out, which is consistent with the tendency of experimental findings [21, 53]. Figure 11(b) shows the clearer correlation between the pedestal degradation and the radial transport; the radial heat and particle flux at $\psi_N = 0.98$ of the LFS midplane start to increase with I_{RMP} while the gradients of both n_e and T pedestals decrease. The n=0 mean pedestal profile is degraded by the plasma response induced by RMP.

The simulation results are compared with experimental data to validate the modeling of RMP. Because of the limitation in the diagnostics, only T_i and V_ϕ from CES measurement are mainly considered. The results are presented in Figure 12. Inverse gradient lengths of the temperature, L_{Ti}^{-1}, (Figure 12(a)) and the toroidal rotation, $L_{V\phi}^{-1}$, (Figure 12(b)) at $\psi_N = 0.98$ are plotted for various RMP coil currents. These are measured for the reference discharge (#18594). In the CES measurement (blue circle), the absolute values of both $\left| L_{Ti}^{-1} \right|$ and $\left| L_{V\phi}^{-1} \right|$ decrease with the external field strength. Although there is ambiguity in the experimental trend, $\left| L_{Ti}^{-1} \right|$ and $\left| L_{V\phi}^{-1} \right|$ seem to decrease by 30% and 38%, respectively, as I_{RMP} increases from 2 kA to 4 kA. In the simulation (orange triangle), L_{Ti}^{-1} shows similar behavior with the experiment. It varies from -6.4 to -4.4 (change of 31%) for the same change in I_{RMP}. We note the simulation result does not include the effect of harmonics with high n (>10) and micro-instabilities on the RMP-driven transport. The assumption of $T_i = T_e$ is also used. Therefore, only the qualitative agreement between experiment and simulation can be evaluated in this figure. For the toroidal rotation, the discrepancy between the measurement and the simulation is found. The change in $L_{V\phi}^{-1}$ with I_{RMP} is small which does not follow the experimental trend where the V_ϕ pedestal is

degraded with increasing I_{RMP}. Disagreement is also found in $\bar{n}_e$ and the stored energy, W_{MHD}. In the experiment, $\bar{n}_e$ is decreased by 2×10^{18} m^{-3} from 3.55×10^{19} m^{-3} and W_{MHD} is reduced by 8% as I_{RMP} increases from 2 kA to 4 kA. However, $\bar{n}_e$ and W_{MHD} decrease by only 1.3×10^{17} m^{-3} and 3% in the simulation, respectively.

The discrepancy between the experimental and the numerical result could result from the limitations of the simulation model. First, this study uses the simplified perpendicular diffusion profile and source models as described in section 2-2. Because the model cannot take into account the exact change of the core plasma transport, degradation of the plasma confinement with RMP can be smaller. Also, the profile stiffness has not been fully reflected in the simulation which is a crucial characteristic of the core transport. For better results, accurate diffusion coefficients and the source profiles based on the experimental data should be considered. In addition, the experimental trend considered in this study appears over 5 seconds in the experiment (see Figure 1(a)), where a significant change in the background conditions (neutral pressure build-up, wall loading, wall temperature, etc.) can occur. These subtle changes can also contribute to the difference between the simulation and the experiment. In this respect, the simulation is expected to become more consistent with the experiment where the RMP current increases rapidly while keeping the background conditions as constant as possible. Second, the edge transport induced by RMP is also underestimated. Previous numerical studies revealed that radial transport at the pedestal region could be increased because of the destabilized micro-instabilities [25, 26, 60] and edge localized ballooning modes [27, 28]. Neoclassical toroidal viscosity transport [61, 62] and magnetic flutter [63, 64] can also be induced by the perturbed magnetic field structure. Besides, we apply the Braginskii model to the parallel transport in the stochastic layer, which can underestimate the radial heat fluxes [65]. Because these effects are not included in this work, the heat and particle flux may be undervalued. Overall, the pedestal degradation in the modeling can be smaller than that of the experimental measurement. Furthermore, the fixed boundary model is used to calculate the RMP field penetration. This condition does not allow the modification of the magnetic perturbation at the boundary. Therefore, it may reduce the field amplification inside the plasma and modification of LCFS, which lessen the change of pedestal profile. In future work, these limitations in the transport and fixed boundary model will be resolved with JOREK-STARWALL [66], which allows the variation of the perturbed field at the boundary.

5. Effects of RMP on PBMs

5-1. Suppression of PBM under RMP

PBMs with $n \leq 14$ are included in the simulation to study the effect of RMP-induced plasma response on PBMs. Note that $n > 14$ modes are also linearly unstable, and the $n = 12$ mode is the most

unstable. Because the growth rate of $n = 10$ is similar to that of $n = 12$ as low n modes are dominant in the nonlinear phase, it is reasonable to exclude $n > 14$ modes to meet the limit of our computing resource. Also, previous numerical modeling [67] revealed that the n = 2 structure induced by RMP suppresses the growth of odd modes and only even modes play a dominant role in the nonlinear phase when RMP is applied. Therefore, $n = 2, 4, 6, 8, 10, 12$, and 14 modes are considered in this study. Nevertheless, one of the important limitations of this study is that only a limited number of even modes are considered.

To study the direct effect of RMP on PBMs, we first calculate the evolution of the $n = 0$ and 2 modes in the presence of RMP for $t \sim 800\tau_A$ with the same method described in section 4. Then, $n = 4, 6, 8, 10, 12$, and 14 are added with an initial amplitude imposed by the coupling with n = 2 to see how PBMs interact with RMP. We note that PBMs are the intrinsic component where n > 2 rather than n = 2 components according to RMP application. The simulation results for the case with I_{RMP} of 2 kA, 3 kA, and 4 kA are presented in Figure 13. The orange dotted line in the figure indicates $W_{kin,max}$ in the natural PBM simulation. For $I_{RMP} = 2$ kA, PBM of n = 6 and 8 exponentially grow in the linear phase and show bursty behaviors at the nonlinear phase. The overall mode amplitude during the nonlinear phase slightly decreases by 30% compared to the Natural ELM case. When RMP of $I_{RMP} = 3$ kA is applied, the overall mode amplitude during the nonlinear phase decreases by 75%. The dominant mode in the linear phase changes to n = 4-6. This is due to the interactions between the n = 2 RMP driven mode and PBMs. It is consistent with the report that the modified field structure induced by RMP changes the dominant mode number to lower n [28]. However, there is still mode crash in the nonlinear phase, and filaments are expelled similarly as in the natural PBM case, but with much smaller amplitudes. Therefore, PBMs are mitigated in this case. On the other hand, PBMs are suppressed with $I_{RMP} = 4$ kA. Most unstable mode changes to n = 4 and shows bursts of very low amplitude only. After then, all modes are saturated and remain stationary without any bursty behavior. Their saturated value is similar to the initial amplitude imposed by the coupling with n = 2. It is noteworthy that ELMs are suppressed in the experiment with $I_{RMP} \sim 3.7$ kA, which agrees fairly well with our modeling results (~ 4 kA). This result is consistent with Ref. [67], where the mode suppression was achieved with the perturbed field, 1.5 times larger than the experimental value.

The effect of RMP on the heat flux at the divertor during ELMs is also investigated. Figure 14 shows the instantaneous ELMy peak heat flux, $Q_{ELM,max}$ ($= Q_{max} - Q_{BG}$) (solid line) and background heat flux, Q_{BG} (dotted line) on the lower-outer divertor plate during the mode crashes. In Figure 14, Q_{BG} has been removed from the actual peak heat flux, Q_{max}, to compare $Q_{ELM,max}$. Here, the time axis for each case is shifted to the left by $0\tau_A$(0 kA), $150\tau_A$(2 kA), $70\tau_A$(3 kA), and $30\tau_A$(4 kA), respectively, to make the comparison easier. When $I_{RMP} = 2$ kA is applied, $Q_{ELM,max}$ decreases by 28% from that

of the natural PBM case. For $I_{RMP} > 2$ kA, $Q_{ELM,max}$ starts to change drastically and eventually decreases by 90% at $I_{RMP} = 4$ kA, where PBMs are suppressed. Because $Q_{ELM,max}$ for $I_{RMP} = 4$ kA is lower than 35 % of the background heat flux, it is negligible. Therefore, we can say that suppression of PBM results in a significant reduction in the heat flux that agrees with the experiments [68, 69].

The background heat flux increases by 50% from the reference value at $I_{RMP} = 4$ kA. It is mainly due to the increased radial transport from the core to SOL, which is consistent with experimental trends [69-71]. Although it is not shown here, the striation pattern of the divertor heat flux is not apparent in our case as tangles induced by RMP [19] are not large enough to affect the heat flux. Detailed analysis of the effect of tangles in divertor heat flux of KSTAR will be pursued as future work. Note that there is a lack of diagnostics, and the KSTAR divertor configuration is not considered accurately in the modeling. As a consequence, a direct comparison of the simulation with the measurement of divertor heat flux is difficult, and it will also be addressed in future works.

The ELMy heat flux during the ELM mitigation is usually smaller [72] than that of natural ELM in the experiments, which is consistent with the above results. However, the simulation result shows the possibility of increased ELMy heat flux during the mitigation phase. It is related to the fact that divertor heat flux depends not only on the amplitude of the mode crash but also n of the most unstable PBM. For example, the peak ELMy divertor heat flux tends to increase as the dominant n becomes lower [73]. Because the amplitude and the dominant n of PBM decrease simultaneously in the ELM mitigation case, the non-monotonic tendency of ELMy heat flux may be observed in the mitigation case. Also, the stochastic field and the tangle structure caused by RMP change the divertor heat flux. However, they cannot be properly considered in this modeling because accurate divertor physics such as neutral recycling, source, and diffusion profiles are not included. Further studies will be required for improving the modeling of the divertor heat flux.

5-2. Effect of mode coupling on the ELM suppression

The crash of PBM is significantly reduced when RMP of sufficient strength is applied. Suppression of PBM with the perturbed field could be related to the degraded mean pedestal which is the source of PBM. It could also result from the increased mode coupling of PBM (n>2) with RMP-induced plasma response (n=2) which has been found in the previous studies [67, 74]. To find the main factor of mode suppression, PBM stability is investigated with the degraded mean density and temperature profile while mode coupling of PBM with RMP is excluded. This is done as the simulation with a pressure gradient and current density modified to the same level as in the ELM suppression case ($I_{RMP} = 4$ kA), but without applying RMPs. As shown in Figure 15(a), the linear growth rate of PBM decreases more

than 60% for all n as compared to the case without pedestal degradation. However, PBMs are still nonlinearly unstable, and significant mode crash occurs despite small growth rates. In Figure 15(b), mode saturation is possible only when mode coupling is included. This indicates that the mode coupling has a dominant effect on the ELM suppression of our case rather than the reduced destabilizing source owing to the pedestal degradation.

Evidence of strong mode coupling between PBMs (n>2) and RMP (n=2) during the mode suppression can be found in Figure 13(c). In the early phase, n=4 mode rapidly grows and reaches $W_{\mathrm{kin}} \approx 0.18$. Then, n=2 mode induced by RMP starts to increase and followed by a decrease of n=4 mode. After that, n=2 mode decreases while n=6 mode starts to grow. Similar patterns are repeated afterwards. There could be energy exchanges between PBMs and the n=2 mode. Here, n=2 mode helps PBMs to share energies among themselves by extracting the energy of the rapidly growing mode and by spreading it to others. Because the energies of PBM are evenly distributed to harmonics, a single mode cannot grow too large to crash. Therefore, RMP acts to increase the coupling between different mode numbers of PBM and results in states with saturated or suppressed modes. In this point of view, this result is consistent with the previous numerical study that the bursty mode crash disappears when mode couplings between PBMs are reinforced [75].

It turns out that the mode coupling can also change the magnitude of the field penetration by RMP. Figure 16 (a) shows δB_{r} and $\delta B'_{\mathrm{r}}$ $(= \partial(\delta B_{\mathrm{r}})/\partial \psi_N)$ of the q = 4 rational surface on the center of the pedestal ($\psi_{\mathrm{N}} \sim 0.98$). Here, δB_r and $\delta B'_{\mathrm{r}}$ are the radial perturbed field strength and its radial gradient of $[m, n] = [8, 2]$ at $t = 3800\tau_{\mathrm{A}}$, respectively. The even parity $\delta B_{\mathrm{r,even}}$ represents the size of the magnetic island, and the odd parity $\delta B'_{\mathrm{r,odd}}$ means the strength of the kink-peeling response. In the figure, $\delta B'_{\mathrm{r,odd}}$ with the mode coupling between PBMs is smaller than the case without it for all I_{RMP}. This is consistent with the decrease in the energy of n = 2 mode when PBMs are included (see Figure 13). This may support that the energy exchange between the n = 2 RMP-driven mode and PBMs is mediated by the n=2 kink-peeling component. On the other hand, $\delta B_{\mathrm{r,even}}$ shows a different behavior. When $I_{\mathrm{RMP}} < 3$ kA, $\delta B_{\mathrm{r,even}}$ has a similar tendency as $\delta B'_{\mathrm{r,odd}}$. On the other hand, for $I_{\mathrm{RMP}} \geq 3$ kA, $\delta B_{\mathrm{r,even}}$ with PBMs becomes larger than the case without it. Once again, ELM suppression is achieved with $I_{\mathrm{RMP}} \sim 4$ kA. To understand the steep increase in $\delta B_{\mathrm{r,even}}$ at $I_{\mathrm{RMP}} \sim 4$ kA, the change in the plasma flow is investigated. Figure 16 (b) shows the perpendicular ExB flow, $V_{\perp,\mathrm{E \times B}}$, and the electron flow, $V_{\perp,\mathrm{e}}$, for the cases with and without PBMs. In the figure, there is no significant flow reduction even with PBMs. Rather, the inclusion of PBMs increases $V_{\perp,\mathrm{e}}$ at the pedestal center, which can reduce the field penetration. Therefore, the increase in $\delta B_{\mathrm{r,even}}$ by PBMs can be more correlated with the mode interaction between the RMP-driven mode and PBMs rather than with the influence of the flow.

Increased $\delta B_{\rm r,even}$ and the island size can further reduce the pedestal gradient. Although it is not shown here, the pedestal gradient further decreases by 8% when the interaction of PBMs and RMP is included. Therefore, the mode coupling effect can also help ELM suppression by enhancing the magnetic island and degrading the pedestal. As the interaction between the magnetic island and PBMs turns out to be important, future work may be needed to consider the plasma resistivity, which should affect magnetic islands and field penetration more strongly than the mode coupling.

5-3. Locking of PBM with RMP

A large change is found in the rotation of the mode when ELM suppression is achieved in the modeling. Figure 17(a) presents the poloidal rotation of the most unstable mode (n>2) for different RMP coil current. Here, $V_{\theta,\rm mode}$ is the poloidal rotation at the midplane of LFS, derived from the simulation in the laboratory frame during the nonlinear phase. In the natural PBM case, a mode shows very oscillatory behavior as the result of nonlinear interaction. The oscillatory behavior of $V_{\theta,\rm mode}$ decreased overall for $I_{\rm RMP} = 2$ kA. For $I_{\rm RMP} = 4$ kA, modes are initially rotating, but start to slow down until they stop rotating at $t \sim 3400\tau_{\rm A}$. They remain nearly static. Unlike $V_{\theta,\rm mode}$, the poloidal $E \times B$ rotation $V_{\theta,\rm E}$ continues to increase. Although it is not shown here, $V_{\theta,\rm E}$ at the center of the pedestal ($\psi_{\rm N} = 0.98$) changes from -3 km/s to -10 km/s in the ion-diamagnetic direction as $I_{\rm RMP}$ increases from 0 kA to 4 kA. It shows that RMP brakes PBMs and this is a prominent feature that distinguishes ELM suppression from mitigation. The sudden braking of ELM after a transition from mitigation to suppression was also observed in the experiments [76, 77]. These experimental results may indicate that the ELM suppression regime consists of static saturated PBMs while natural or mitigated regimes consist of rotating PBMs. Unfortunately, the mechanism of the mode braking is unclear. The previous numerical study [67] tried to explain the mode braking with the RMP-induced electromagnetic torque [14]. The reduction of perpendicular electron flow is also observed in our modeling which is consistent with this study. However, there is no direct evidence and quantitative explanations for mode braking with RMP-induced torque yet. Another possible candidate is the interaction between the mode and the magnetic island. In Figure 17 (a), the magnetic island and $\delta B_{\rm r,even}$ rapidly increase at $I_{\rm RMP} \sim 4$ A, where the mode locking occurs. The rapid increase in $\delta B_{\rm r,even}$ implies a strong coupling between PBMs and the magnetic island, so the perturbed field and the coupling effect may have influenced the suppression of mode rotation. In addition, the interaction of the resonant currents with the external fields can also be important because it affects the torque balance with RMP. Further analysis is needed as future work.

To understand the role of mode braking in the ELM suppression, we investigate the effect of $V_{\theta,\rm mode}$ to the mode coupling and ELM suppression for the first time. In our modeling, perturbed quantities ($X_{\rm n}$)

of a single harmonic is described as

$$X_n(R, Z, \phi) = X_n(R, Z) \cos[n\phi + \delta_n(R, Z)]. \tag{11}$$

In Eq. (11), $X_n(R, Z)$ and the cosine term catch the poloidal and the toroidal variations of mode, respectively. The mode coupling is affected by their relative spatial position and it is related to the relative phase difference, $\Delta\delta(= \delta_n - \delta_{n'})$. In the previous section, we concluded that the suppression of PBM may result from energy exchange between n=2 RMP-induced mode and PBMs (n>2). Steady energy transfer between modes is vital in this respect. However, energy transfer will be suppressed if $\Delta\delta$ keeps changing. For example, when we consider the momentum equation, nonlinear terms in $\partial_t u_n$ depends on $\cos[\delta_{n1} - \delta_{n2}]$ where $n = n_1 - n_2$. Because $\partial_t W_{kin}$ for n is proportional to $u_n \partial_t u_n$, it is also affected by $\Delta\delta(= \delta_{n1} - \delta_{n2})$. In addition, the time scale of $\Delta\delta$ is $\sim 100\tau_A$ comparable to that of mode fluctuations. Therefore, $\Delta\delta$ should remain constant to maintain consistent energy exchange between modes. It is equivalent to keeping the spatial overlapping of mode structures. Because the RMP-induced n=2 mode is static in space, $\Delta\delta$ only depends on $V_{\theta,mode}$ of PBM. To keep $\Delta\delta$ constant, $V_{\theta,mode}$ needs to be very small, and mode locking can be advantageous to ELM suppression. In Figure 17(b), the phase difference ($\Delta\delta$) between n=2 (RMP) and the largest harmonic of PBM at the midplane of LFS is presented. During the nonlinear phase, it clearly shows how $V_{\theta,mode}$ affects $\Delta\delta$. When $I_{RMP} = 1$ kA or 2 kA, $\Delta\delta$ shows considerable variation because of the oscillatory $V_{\theta,mode}$ as shown in Figure 17(a). For $I_{RMP} = 4$ kA (ELM suppression case), however, $\cos\Delta\delta$ remains almost constant (~ -0.8) with locking of PBM. Therefore, it can be suggested that PBM locking by RMP increases the coupling of RMP and PBMs, resulting in mode suppression.

In the nonlinear phase, $V_{\theta,mode}$ can be expressed as

$$V_{\theta,mode} \approx V_{\theta,E} + V_{\theta,NL}, \tag{12}$$

where $V_{\theta,NL}$ is the poloidal mode rotation generated by nonlinear interactions including RMP. We note that when $V_{\theta,E}$ increases, more I_{RMP} can be needed to drive $V_{\theta,NL}$ to make $V_{\theta,mode}$ vanish. Locking PBMs with RMP becomes more difficult with larger $V_{\theta,E}$. In this context, large $V_{\theta,E}$ will be disadvantageous to ELM suppression. To test this hypothesis, the effect of RMP on PBMs with increased $V_{\theta,E}$ is investigated. In this simulation, the n=0 component of $V_{\theta,E}$ at the center of the pedestal is increased from -3 km/s to -15 km/s while other conditions are fixed. The modified radial profile of $V_{\theta,E}$ at the edge region is shown in Figure 18(a). $W_{kin,max}$ of PBM in the nonlinear phase with corresponding I_{RMP} is presented in Figure 18(b). For the case of modified $V_{\theta,E}$, the mode amplitude remains almost constant for the natural and mitigated PBM cases. At $I_{RMP} = 4$ kA, the suppression of the mode is not achieved and locking of PBM does not occur either. While the pressure

gradient at the center of pedestal decreases by 35%, it decreases by 28% in the case with the modified $V_{\theta,E}$ profile. When $V_{\theta,E}$ is modified, the $V_{\perp,e} = 0$ layer is pushed outward from $\psi_N = 0.95$ to 0.97, and the radial width of the stochastic layer is reduced. Thus, the degradation of the pedestal is relatively small. Our results showed that mode coupling plays a more critical role in ELM suppression than the reduction of the pedestal gradient. Therefore, the locking of PBM ($V_{\theta,mode} \to 0$) is the main factor for the ELM suppression. Furthermore, small $V_{\theta,E}(\approx 0)$ in the pedestal region will be advantageous in terms of PBM locking. It might be related to the importance of $V_{\theta,E} \approx 0$ in ELM suppression in experiments [78].

We also found W_{kin} of n=2 plasma response for the applied RMP increases for modified $V_{\theta,E}$. It is possibly due to the increased radial shear of $V_{\theta,E}$ which can destabilize the n=2 KPM. As it gets closer to the stability limit, RMP can induce larger plasma response. Similar phenomenon was found in the numerical studies on QH-mode [79, 80], where KPM (or Edge Harmonic Oscillation) was destabilized by the large E×B shearing rate. Therefore, $V_{\theta,E}$ can also affect the ELM suppression in terms of the plasma response induced by RMP.

6. Conclusion

With nonlinear modeling, we investigated the effect of n=2 RMP on the plasma equilibrium and PBMs in KSTAR. As RMP penetrated into the plasma, it induced the kink-tearing response including KPM and magnetic islands on the plasma equilibrium. The plasma deformation and radial $E \times B$ convective flux occurred at the pedestal by KPM. When RMP is applied, the external field was almost shielded in the plasma core, while considerable field penetration was observed at the plasma edge as finite plasma resistivity in this region reduced the shielding effect. For our reference KSTAR equilibrium, $V_{\perp,e} = 0$ at the pedestal top ($\psi_N = 0.95$) strengthened the field penetration at the rational surface near the pedestal. As a consequence, a stochastic layer was formed in $\psi_N = 0.95{\sim}1.0$. The radial heat and the particle flux are increased with these plasma responses. They resulted in reduced of the pedestal gradient. Degradation of the temperature pedestal showed good qualitative agreement between the modeling and the experimental results. However, changes in the toroidal rotation and density pedestal are underestimated in the simulation. A more accurate diffusion and source model will be needed to resolve these discrepancies.

The modeling of PBMs with RMP showed that sufficient RMP could suppress PBMs. In KSTAR discharge #18594, RMP with $I_{RMP} = 2$ kA mitigated the bursty mode crashes, while the mode suppression was achieved at $I_{RMP} = 4$ kA. ELMs were suppressed for $I_{RMP} \gtrsim 3.7$ kA in the experiment which agrees well with the modeling results. In our study, the mode coupling between PBMs

and n=2 mode induced by RMP plays a more crucial role in ELM suppression than the mean pedestal degradation. RMP acts to enhance the coupling between the harmonics of PBM and prevents a single mode from overgrowing. In addition, the mode coupling effect increases the magnetic islands in the pedestal, further reducing the pedestal gradient. It leads to saturation of modes rather than the crash of a mode. Our analysis shows that the kink-peeling component with odd parity is important in exchanging the energy between modes. In this regard, an operational regime that maximizes the kink-peeling response is more efficient for ELM suppression. This is consistent with previous results [21, 53, 81] that the kink-peeling mode is observed in ELM suppression discharges. However, additional work will be needed to gain insight into the operational windows for ELM suppression, in terms of q95, plasma shape, etc.

The locking of PBM was observed during the mode suppression. It was the major difference between the mitigation and the suppression cases. We propose a model to explain the positive effect of PBM locking on the mode coupling and suppression for the first time. In our explanation, small $V_{\theta,mode}$ or $V_{\theta,E}$ at the pedestal is advantageous to ELM suppression as a constant phase difference of modes can enhance the couplings between PBMs and RMP. It might be related to some experimental cases where $V_{\theta,E} \approx 0$ plays a significant role in ELM suppression. Further work will be done to advance the RMP modeling to understand the mechanism of ELM suppression which will propose a reliable ELM-suppression criterion for ITER.

Acknowledgements

References

[1] H. Biglari, P.H. Diamond and P.W. Terry, Phys. Fluids B 2 (1990) ,1

[2] T. S. Hahm and K.H. Burrell, Phys. Plasmas 2 (1995), 1648

[3] C. D. Challis et al., Nucl. Fusion 55 (2015), 053031

[4] J. W. Connor et al., Phys. Plasmas 5 (1998), 2687

[5] P. B. Snyder et al., Nucl. Fusion 44 (2004), 320

[6] A. Loarte et al, Plasma Phys. Controlled Fusion 45 (2003), 1549

[7] G. T. A Huysmans et al, Nucl. Fusion 53 (2013), 123023

[8] T. E. Evans et al., PRL 92 (2004), 235003

[9] Y. M. Jeon et al., PRL 109 (2012), 035004

[10] Y. Sun et al., PRL 117 (2016), 115001

[11] W. Suttrop et al., Plasma Phys. Control. Fusion 59 (2017), 014049

[12] Y. Liang et al., PRL 98 (2007), 265004

[13] A. Kirk et al., PRL 108 (2012), 255003

[14] R. Fitzpatrick et al., Phys. Plasmas 5 (1998), 3325

[15] M. Heyn et al., Nucl. Fusion 54 (2014), 064005

[16] E. Nardon et al., Nucl. Fusion 50 (2010), 034002

[17] M. Becoulet et al., Nucl. Fusion 52 (2012), 054003

[18] N. M. Ferraro et al., Phys. Plasmas 19 (2012), 056105

[19] F. Orain et al., Phys. Plasmas 20 (2013), 102510

[20] R. Nazikian et al., PRL 114 (2015), 105002

[21] C. Paz-Soldan et al., PRL 114 (2015), 105001

[22] Y. Liu et al., Nucl. Fusion 58 (2016), 114005

[23] N. M. Ferraro et al., Nucl. Fusion 53 (2013), 073042

[24] F. Orain et al., Nucl. Fusion 57 (2017), 022013

[25] T. M. Bird et al., Nucl. Fusion 53 (2013), 013004

[26] I. Holod et al., Nucl. Fusion 57 (2017), 016005

[27] M. Willensdorfer et al., PRL 119 (2017), 085002

[28] M. L. Mou et al., Physics of Plasma 25 (2018), 082518

[29] G. T. A Huysmans et al., Plasma Phys. Control. Fusion 51 (2009), 124012

[30] T.A.Gianakon et al., Phys. Plasams 9 (2002), 536

[31] C.E.Kessel et al., Nucl. Fusion 34 (1994), 1221

[32] M. Becoulet et al., Nucl. Fusion 57 (2017) 116059

[33] O. Czarny and GTA Huijsmans, Journal of Comp. Phys. 227 (2008), 7423

[34] Henon P. et al., Parallel Comp. 34 (2008), 318

[35] J. Lee et al., Nucl. Fusion 59 (2019), 066033

[36] Yun. G.S, RSI, V81 10D930(2010)

[37] Yun. G.S, RSI, V85 11D820(2014)

[38] L. L. Lao et al., Nucl. Fusion 25 (1985), 1611

[39] S. A. Lazerson et al., Plasma Phys. Control. Fusion 55 (2013), 084004

[40] S. A. Lazerson et al., Nucl. Fusion 55 (2015), 023009

[41] A. Wingen et al., Nucl. Fusion 57 (2017), 016013

[42] Kim M. et al., Nucl. Fusion 54 (2014) 093004

[43] R. Hager and C. S. Chang, Phys. Plasmas 23 (2016), 042503

[44] A.B. Mihailovskii. et al., Plasma Phys. Rep. 23 (1997), 844

[45] S. Saarelma et al., Plasma Phys. Control. Fusion 60 (2018), 014042

[46] J. Morales, Phys. Plasmas 23 (2016), 042513

[47] I. Krebs et al., Phys. Plasmas 20 (2013), 082506

[48] S. Pamela et al., Plasma Phys. Control. Fusion 58 (2016), 014026

[49] M. Becoulet et al., Nucl. Fusion 48 (2008), 024003

[50] P.B. Snyder, et al., Nucl. Fusion 47 (2007), 961

[51] R. A. Moyer et al., Nucl. Fusion 52 (2012), 123019

[52] Daisuke Shiraki et al., Phys. Plasmas 20 (2013), 102503

[53] C. Paz-Soldan et al., Nucl. Fusion 56 (2016), 056001

[54] E. Nardon et al., Phys. Plasmas 14 (2007), 092501

[55] M. Leconte and J.-H. Kim et al., Phys. Plasmas 22 (2015), 082301

[56] Y. Liu et al., Phys. Plasmas 17 (2010), 122502

[57] S. R. Haskey et al., Plasma Phys. Control. Fusion 57 (2015), 025015

[58] G. T. A. Huysmans et al., Plasmas Phys. Control. Fusion 47 (2005), 2107

[59] Y. Liu et al., Nucl. Fusion 51 (2011), 083002

[60] G.J, Choi and T.S. Hahm., Nucl. Fusion 58 (2018), 026001

[61] W. Zhu et al., PRL 96 (2006), 225002

[62] J.-K. Park et al., Phys. Plasmas 16 (2009), 056115

[63] F. L. Waelbroeck et al., Nucl. Fusion 52 (2012), 074004

[64] J.D. Callen et al., Nucl. Fusion 53 (2013), 113015

[65] T. Rhee et al., Nucl. Fusion 55 (2015), 032004

[66] M Hölzl et al., Journal. Phys: Conf. Series 401 (2012), 012010

[67] F. Orain et al., Phys. Plasmas 26 (2019), 042503

[68] T. E. Evans et al., Journal of Nucl. Materials 337-339 (2005), 691

[69] M. W. Jakubowsku et al., Nucl. Fusion 49 (2009), 095013

[70] A. J. Thornton et al., Nucl. Fusion 54 (2014), 064011

[71] Y. In et al., Nucl. Fusion 57 (2017), 116054

[72] A. J. Thornton et al., Journal of Nucl. Materials 438 (2013), S199

[73] J.-W. Ahn et al., Nucl. Fusion 54 (2014), 122004

[74] M. Becoulet et al., PRL 113 (2014), 115001

[75] P. W. Xi, et al., PRL 112 (2014), 085001

[76] J. Lee et al., PRL 117 (2016), 075001

[77] J. Lee et al., "Bifurcation of perpendicular rotation and field penetration at the transition to RMP induced ELM crash suppression," Preprint: 2018 IAEA Fusion Energy Conference, Gandhinagar [p.EX/P7-13]

[78] C. Paz-Soldan et al., Nucl. Fusion 59 (2019), 056012

[79] G.S. Xu et al., Nucl. Fusion 57 (2017), 086047

[80] F. Liu et al., Plasma Phys. Control. Fusion 60 (2018), 014039

[81] A. Wingen et al., Nucl. Fusion 54 (2014), 064007
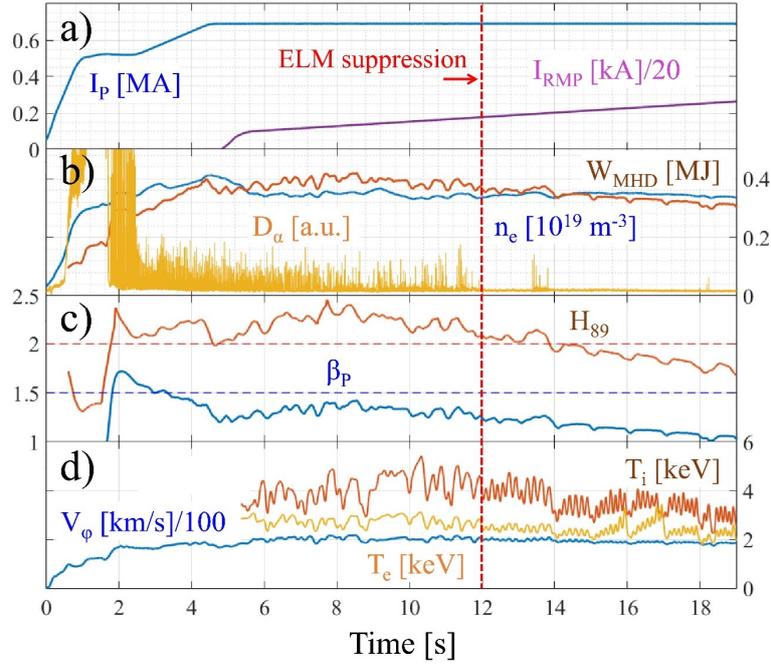
Figure 1. Time evolution of (a) plasma current, I_p, RMP coil current, I_RMP, (b) D_α signal, line average density, $\bar{n}_\mathrm{e}$, stored energy, W_MHD, (c) H_{98}, poloidal beta, β_p, (d) ion temperature, T_i, electron temperature, T_e, and toroidal plasma rotation, V_ϕ in core of the KSTAR discharge #18594.
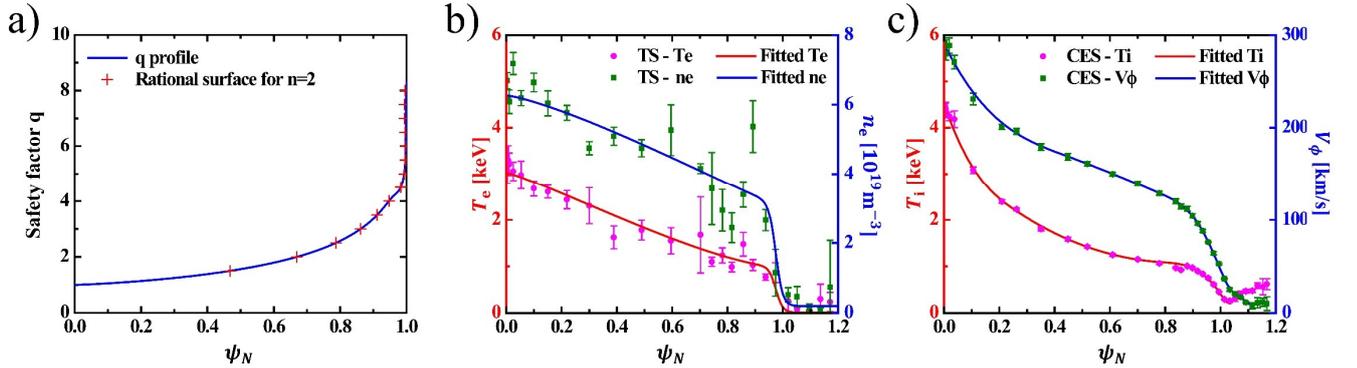
Figure 2. (a) Radial profile of safety factor q (blue line) and position of rational surface (red dot) with n=2. (b) Radial profiles of electron temperature, T_e (red line), and electron density, n_e, (blue line) taken in modeling, with the experimental measurements of T_e (red dot) and n_e (green dot). (c) Radial profiles of ion temperature, T_i (red line), and toroidal rotation velocity, V_ϕ (blue line), taken in modeling, with the experimental measurements of T_i (red dot) and V_ϕ (green dot).
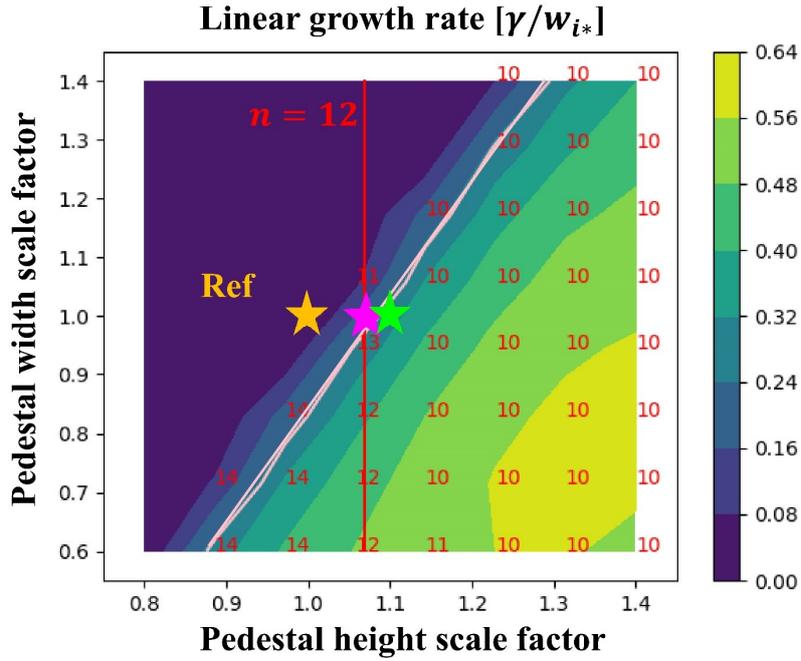
Figure 3. The linear growth rate of PBM of the most unstable mode in pedestal height and width space is presented. The mode number of most unstable mode is also shown. The pink line is the marginal PBM stability limit, and the red line corresponds to the pedestal whose dominant PBM mode has n = 12. Yellow star, pink star, and green star represent the reference point, the intersection of the pink and red line, and the newly fitted pedestal, which is used in the modeling, respectively.
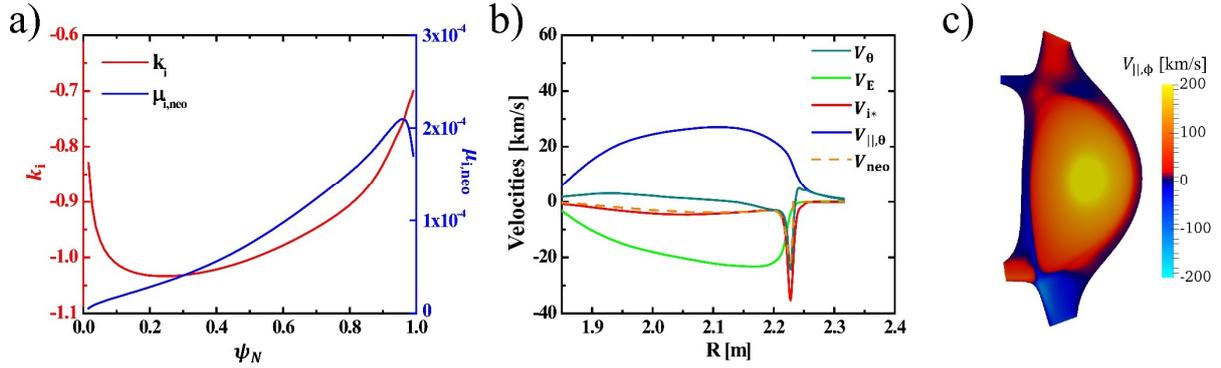
Figure 4. (a) Radial profiles of neoclassical coefficients, k_i (red line) and $\mu_{i,neo}$ (blue line). (b) Radial profiles of poloidal velocity V_θ at the midplane of LFS with $E \times B$ (V_E, green line), ion diamagnetic (V_{i*}, red line), parallel ($V_{\|\theta}$, blue line), and neoclassical (V_{neo}, orange line) components. (c) Poloidal distribution of toroidal plasma rotation velocity, $V_{\|\phi}$,.
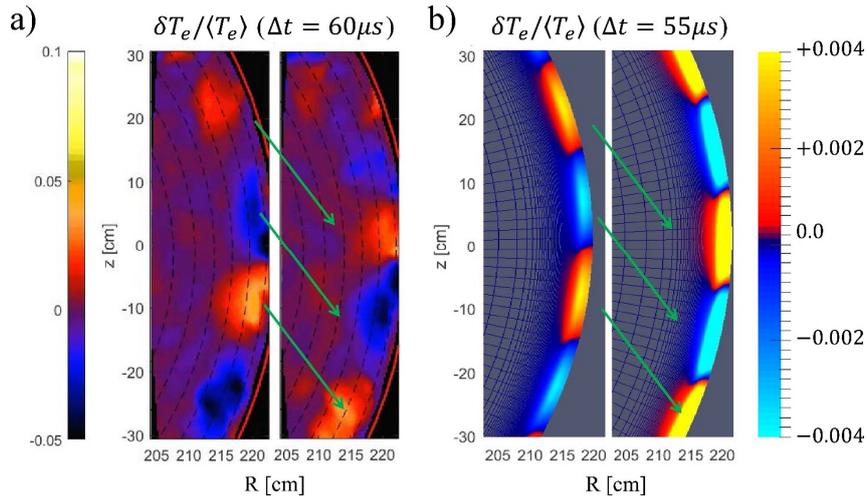
Figure 5. (a) 2D measurement of electron temperature fluctuation in R-Z space from ECEI diagnostics (n=12) in the LFS region at consecutive times slices of $\Delta t = 60$ μs. (b) Simulation result of electron temperature fluctuation at two different time slices with $\Delta t = 55$ μs near the onset of mode crash.
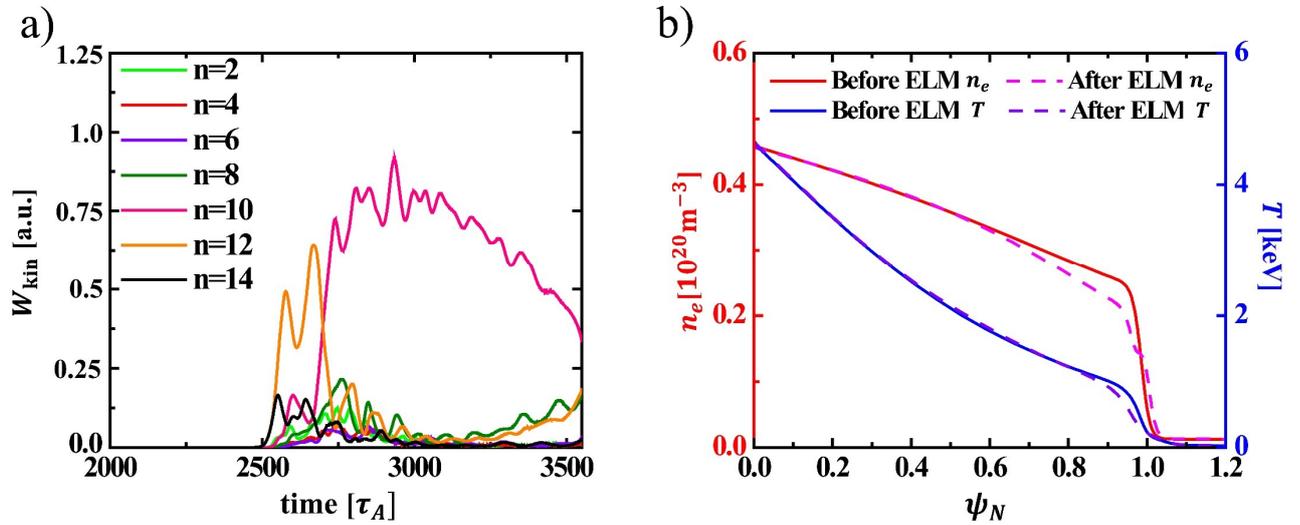
Figure 6. (a) Time evolution of the toroidal harmonics of the kinetic energy for n=2~10. (b) Comparison of n_e and T_e before the onset of ELM ($\sim 2500\tau_A$) and after the crash ($\sim 3500\tau_A$). They show the nonlinear phase of natural PBM without RMP.
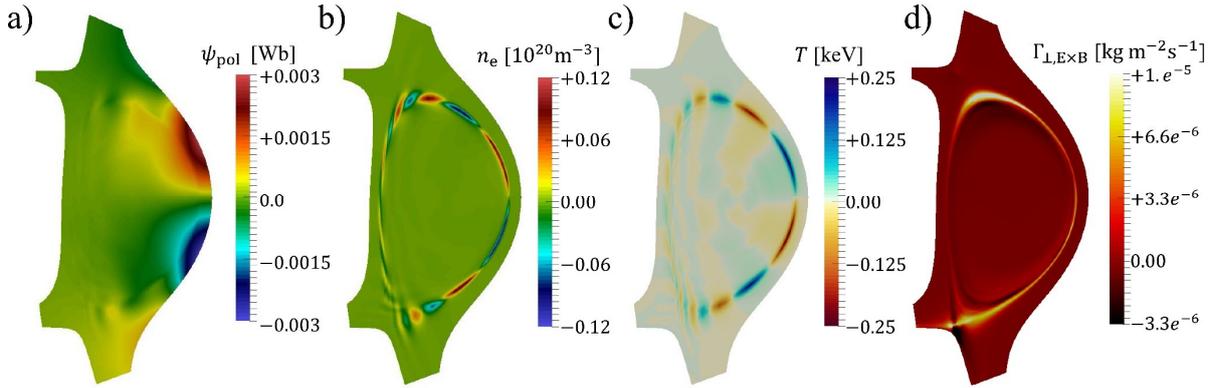
Figure 7. Poloidal distribution of (a) n=2 magnetic flux ψ_{pol}, (b) n_{e}, and (c) T perturbation induced by RMP. (d) n=0 $\mathrm{E \times B}$ radial flux, $\Gamma_{\perp,\mathrm{E \times B}}$, which is driven by the RMP-induced plasma response.
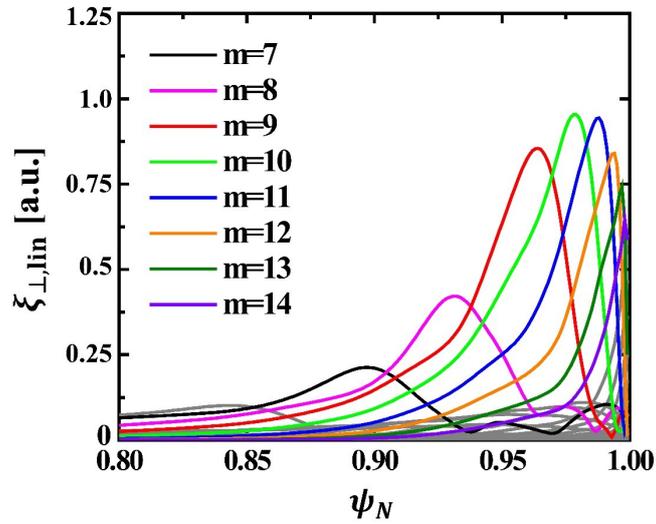
Figure 8. Radial mode structure of the plasma displacement $\xi_{\perp,\mathrm{lin}}$ induced as a response to RMP. The mode structure is highly localized at the plasma edge, which is the typical structure of KPM.
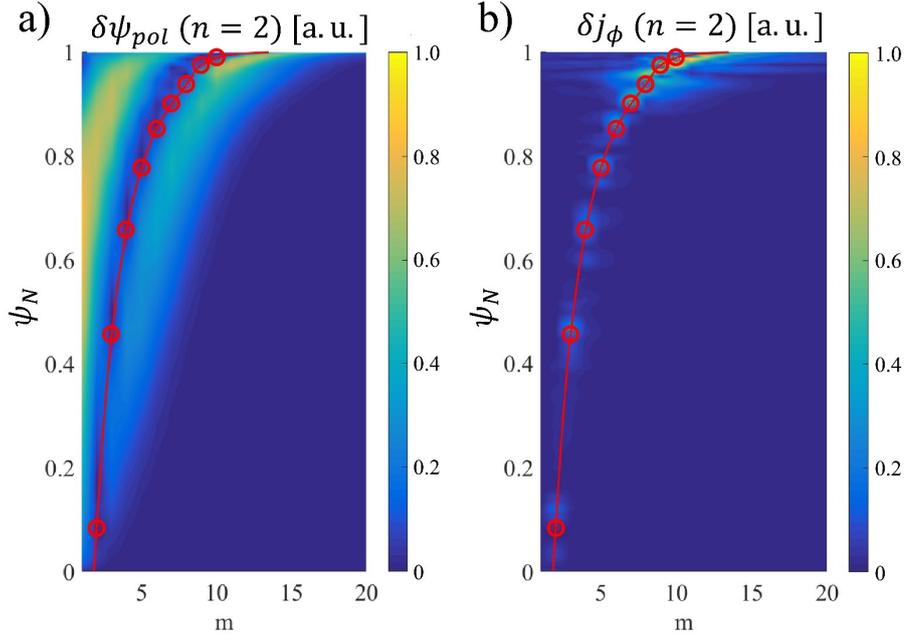
Figure 9. Perturbed n=2 components of the (a) poloidal magnetic flux $\delta\psi_{\text{pol}}$ and (b) current δj_ϕ as functions of the poloidal mode number m and the normalized flux ψ_N are presented. In each figure, resonant surfaces are plotted with the red line and circles.
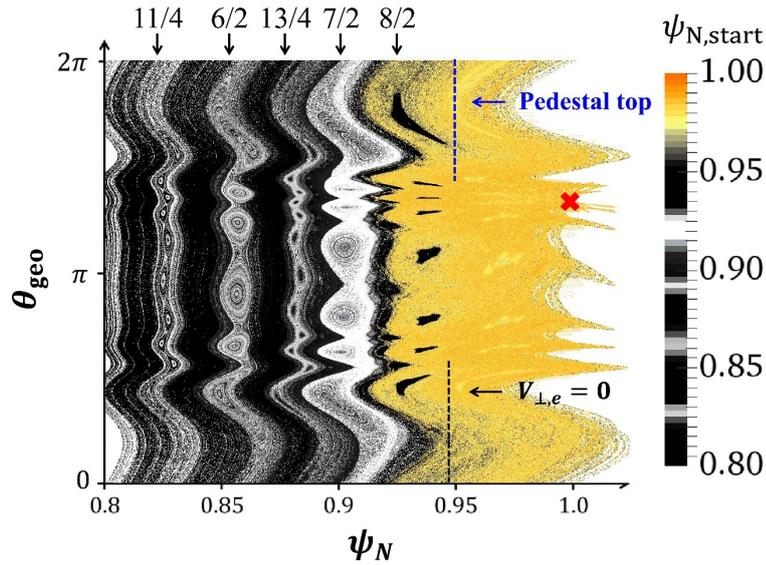
Figure 10. Poincare plot of the perturbed magnetic structure in ψ_N and poloidal θ_{geo} coordinate is presented. The stochastic layer is formed at $0.95 \leq \psi_N \leq 1.0$. Here, the color values represent ψ_N of the starting point of field line tracing. The positions of pedestal top, $V_{\perp,e} = 0$, and X-point are represented by the blue dotted line, black dotted line, and red cross, respectively.
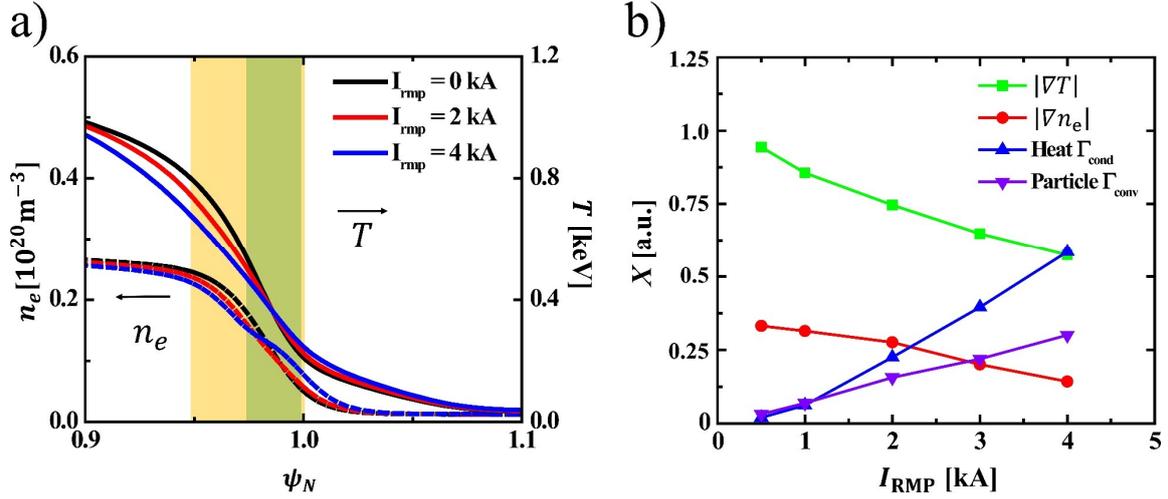
Figure 11. (a) n=0 profile degradation of n_e and T pedestal, which is induced by RMP. The yellow and green colored regions highlight the radial width of the stochastic layer and $E \times B$ convection layer, respectively. (b) The radial gradient of n_e (red dotted line) and T (blue dotted line) at the center of the pedestal ($\psi_N = 0.98$) with varying I_{RMP}. The conductive heat flux Γ_{cond} and convective particle flux Γ_{conv} at the same location are also presented.
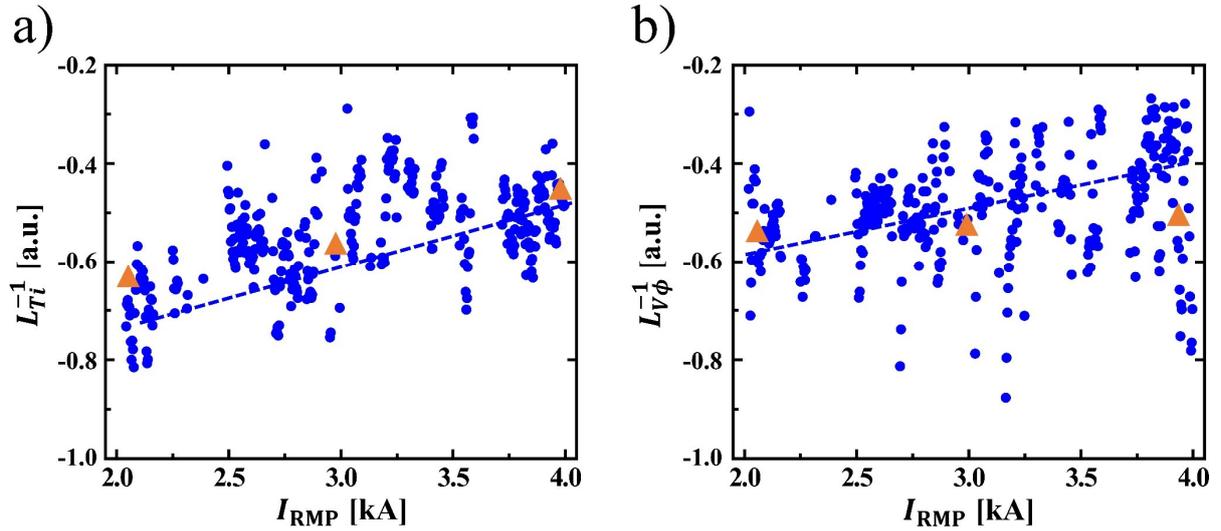
Figure 12. Experimental measurement for KSTAR shot #18594 of inverse gradient length of (a) ion temperature, L_{Ti}^{-1}, and (b) toroidal plasma rotation, $L_{V\phi}^{-1}$, with increasing I_{RMP} are presented (blue dot). The blue dotted line corresponds to the trend line. Simulation results are plotted as orange triangles in each figure.
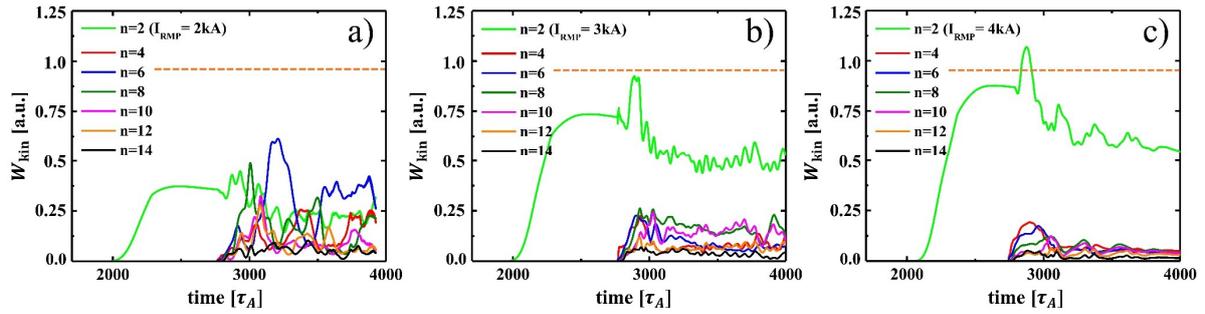
Figure 13. Time evolution of the toroidal harmonics of the kinetic energy for n=2~10 is presented. Each figure corresponds to the case of PBM with I_{RMP} equals to (a) 2 kA, (b) 3 kA, and (c) 4 kA. Units are arbitrary, but the normalization is the same in all cases. The orange dotted line represents the maximum W_{kin} in the natural ELM simulation. Here, n=2 mode is the RMP-induced mode.
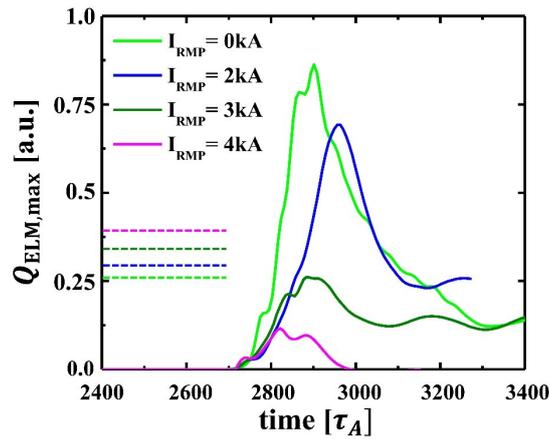

Figure 14. Time evolution of the ELMy heat flux (solid line) and background heat flux (dotted line) on the lower divertor of the LFS for various I_{RMP} are presented. It shows that ELMy heat flux decreases with I_{RMP} while background heat flux increases.
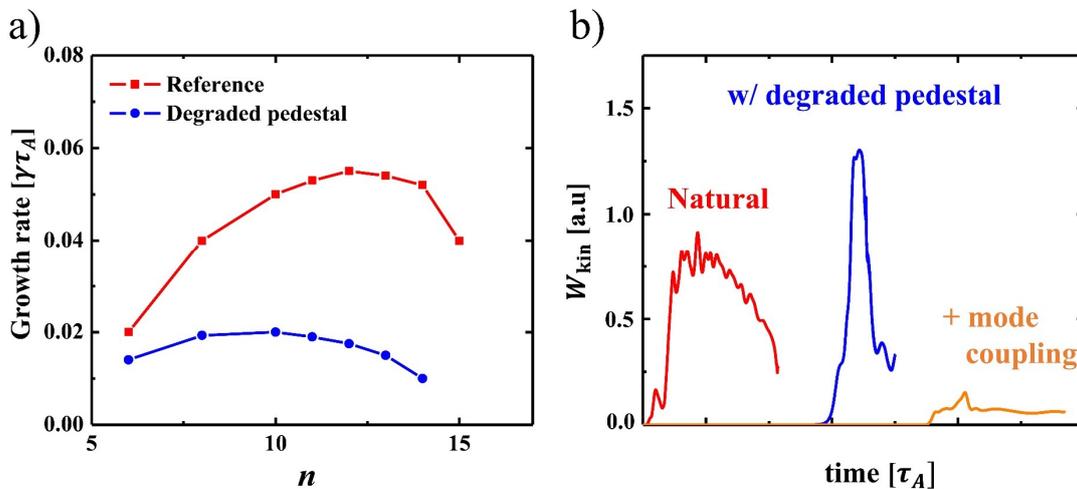

Figure 15. (a) Spectrum of the linear growth rate. The red line and blue line correspond to the growth rate of PBM for reference equilibrium and for that with degraded pedestal induced by RMP, respectively. (b) Nonlinear evolution of W_{kin} of n=10 component for the natural PBM (red line), for PBM with degraded pedestal (blue line), and for PBM with mode coupling including RMP (orange line).
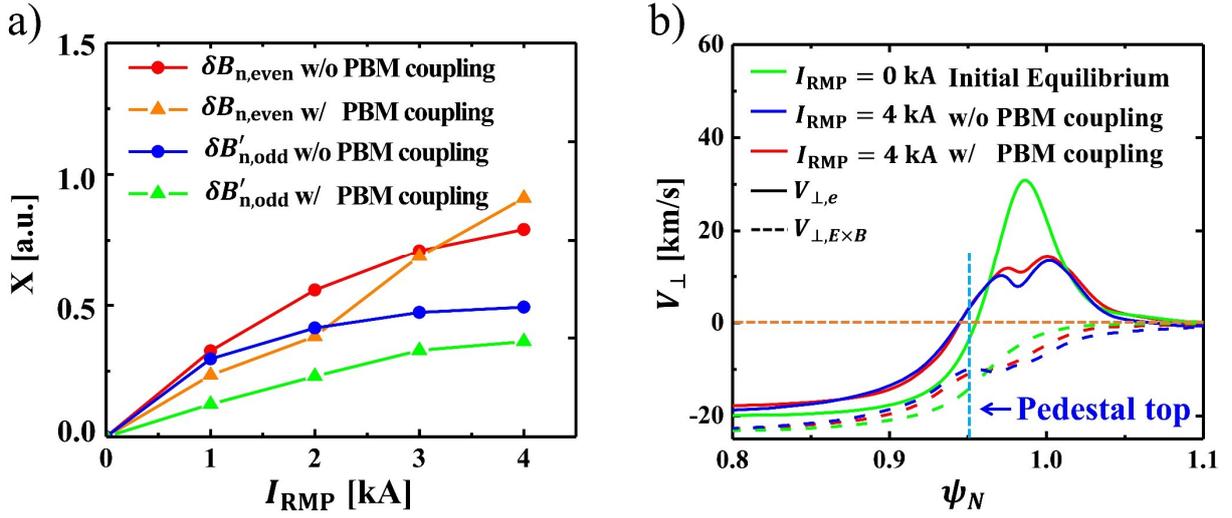
Figure 16. a) $\delta B_{r,even}$ and $\delta B'_{r,odd}$ of $[m, n] = [8,2]$ on the $q=4$ rational surface for various I_{RMP}. The red line and orange line correspond to the radial perturbed field strength of even parity, $\delta B_{r,even}$, with and without mode coupling between PBMs, respectively. The blue line and green line represent the radial gradient of the perturbed field strength of odd parity, $\delta B'_{r,odd}$, with and without PBM, respectively. (b) The radial profile of the ExB flow, $V_{\perp,E \times B}$ (dotted line), and electron flow, $V_{\perp,e}$ (solid line). The green color corresponds to the initial equilibrium case. The red and blue colors represent the cases with and without PBM, respectively. The orange dotted line corresponds to $V_\perp = 0$.
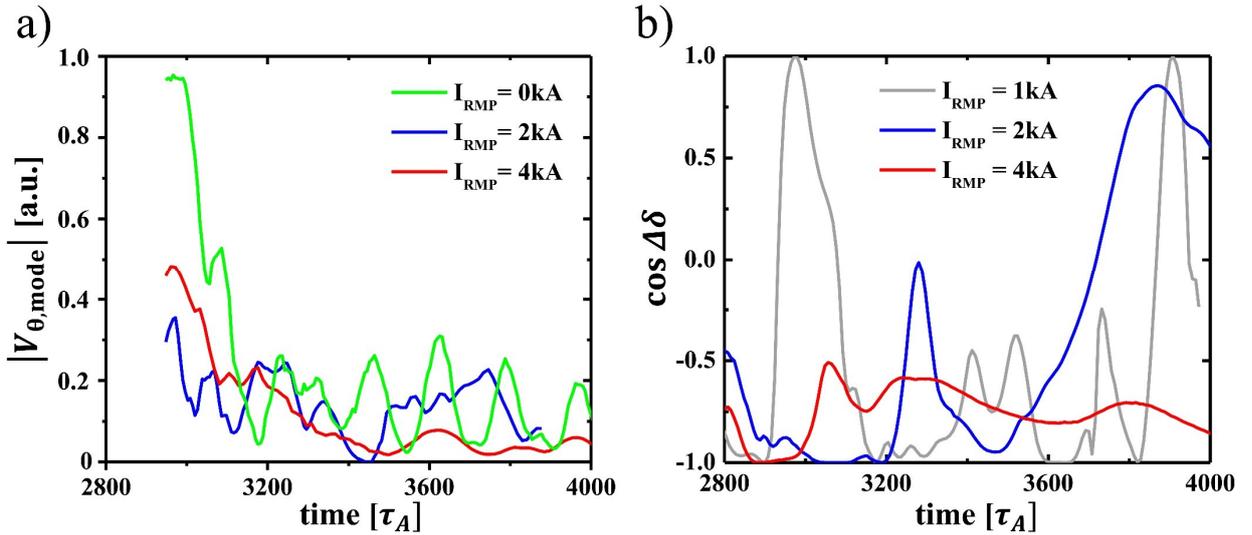

Figure 17. a) Time evolution of the poloidal mode rotation $V_{\theta,mode}$ during the nonlinear phase. It shows $V_{\theta,mode}$ of the natural PBM (n=12, green line), PBM with $I_{RMP} = 2$ kA (n=6, blue line), and $I_{RMP} = 4$ kA (n=4, red line). (b) Time evolution of $\cos \Delta\delta$, where $\Delta\delta$ is the phase difference between n=2 RMP-induced mode and the most unstable harmonic component of PBM for I_{RMP} of 1 kA (n=6, green line), 2 kA (n=6, blue line), and 4 kA (n=4, red line).
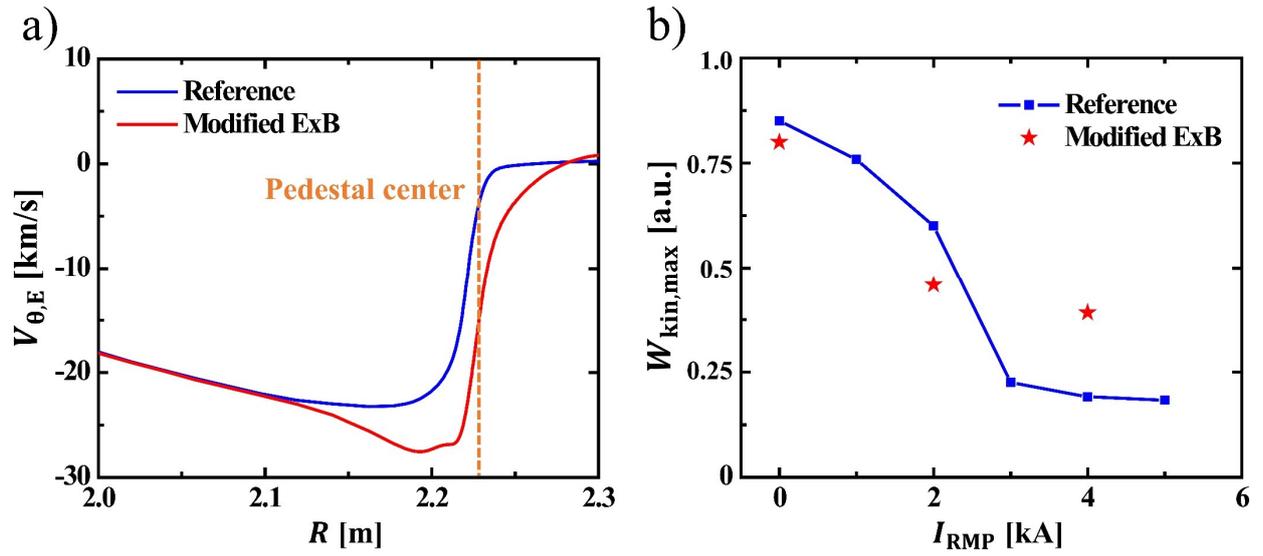
**Figure 18.** a) Radial profile of E × B poloidal rotation profile at the midplane of LFS. Profile of reference case (blue line) and modified case (red line) are presented. Here, the orange dotted line corresponds to the position of the pedestal center, and ion-diamagnetic flow is in (the negative) direction. (b) The largest kinetic energy of PBM during the nonlinear phase for various I_{RMP}. The blue dotted line and red stars correspond to the reference and modified cases, respectively.